YALE PEABODY MUSEUM

JOURNAL OF MARINE RESEARCH

The *Journal of Marine Research,* one of the oldest journals in American marine science, published important peer-reviewed original research on a broad array of topics in physical, biological, and chemical oceanography vital to the academic oceanographic community in the long and rich tradition of the Sears Foundation for Marine Research at Yale University.

An archive of all issues from 1937 to 2021 (Volume 1–79) are available through EliScholar, a digital platform for scholarly publishing provided by Yale University Library at https://elischolar.library.yale.edu/.

Requests for permission to clear rights for use of this content should be directed to the authors, their estates, or other representatives. The *Journal of Marine Research* has no contact information beyond the affiliations listed in the published articles. We ask that you provide attribution to the *Journal of Marine Research.*

Yale University provides access to these materials for educational and research purposes only. Copyright or other proprietary rights to content contained in this document may be held by individuals or entities other than, or in addition to, Yale University. You are solely responsible for determining the ownership of the copyright, and for obtaining permission for your intended use. Yale University makes no warranty that your distribution, reproduction, or other use of these materials will not infringe the rights of third parties.

Three-dimensional stirring of thermohaline fronts

by Patrice Klein[1], Anne-Marie Treguier[1] and Bach Lien Hua[1]

ABSTRACT

This study investigates the stirring of the thermohaline anomalies in a fully turbulent quasi-geostrophic stratified flow. Temperature and salinity fields are permanently forced at large scales and are related to density by a linear equation of state. We show, using some inherent properties of quasi-geostrophic turbulence, that the 3-D ageostrophic circulation is the key dynamical characteristic that governs the strength and the spatial distribution of small-scale thermohaline fronts that are strongly density compensated. The numerical simulations well illustrate the formation by the mesoscale eddy field of sharp thermohaline fronts that are mainly located in the saddle regions and around the eddy cores and have a weak signature on the density field. One important aspect revealed by the numerical results is that the thermohaline anomalies experience not only a direct horizontal cascade but also a significant vertical cascade. One consequence of this 3-D cascade is that the ultimate mixing of the thermohaline anomalies will not be necessarily maximum at the depth where the large-scale temperature and salinity anomalies are maximum. Some analytical arguments allow us to identify some of the mechanisms that drive this 3-D cascade.

1. Introduction

Experimental data display abundant examples of small-scale thermohaline features, of a few kilometers, characterized by a strong density compensation between temperature and salinity gradients (see for example: Roden, 1977; Arhan, 1990; Yuan and Talley, 1992; Arhan and King, 1995; Park and Gamberoni, 1997). One explanation of these observations is that the large-scale thermohaline anomalies are broken up by the mesoscale eddies, yielding strong small-scale thermohaline fronts on which diffusive processes are active and efficient. A detailed understanding of the production and spatial distribution of these thermohaline fronts is important to better assess the order of magnitude of the mixing of the thermohaline anomalies.

Chen and Young (1995) have proposed a convincing explanation for the appearance of compensated thermohaline fronts within the mixed layer that is based on a combination of the horizontal mesoscale stirring processes with a nonlinear parameterization of the diffusion coefficient. For the ocean interior where the diffusion is quite small, a heuristic and *qualitative* argument, proposed by MacVean and Woods (1980) for a specific situation which involves a region of normal strain rate, is often invoked to explain the larger strength of the thermohaline fronts when compared to the density fronts. This argument, which is

---

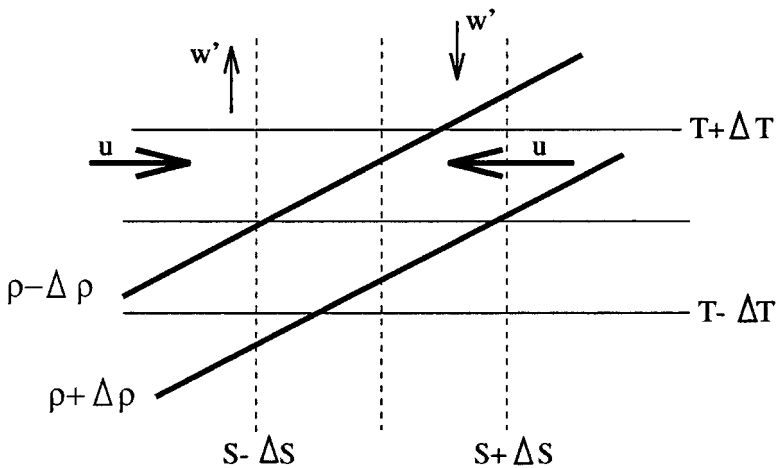1. Laboratorie de Physique des Océans, IFREMER, 29280 Plouzané, France.

Figure 1. In this area of normal strain rate ($\partial u/\partial x < 0$) the motions ($u$, w'), almost parallel to the isolines of the density field (that is a combination of a temperature field and a salinity field), are not an effective mechanism for increasing horizontal density gradients. However they are efficient enough to increase the gradients of temperature and salinity whose isopleths are inclined to the isopycnals.

illustrated in Figure 1, states that motions within the ocean interior are almost parallel to the isopycnals. The consequence is that they are not an effective mechanism for increasing horizontal density gradients but are efficient enough to increase the gradients of properties whose isopleths are inclined to the isopycnals.

The purpose of this study is to revisit the question of the formation and evolution of both the mesoscale and small-scale thermohaline anomalies that are strongly density compensated in the ocean interior. It attempts to extend and rationalize some of the concepts developed in previous studies to the case of a time evolving, fully turbulent, 3-D eddy field. Since the dynamics within the ocean interior are quasi-geostrophic, our rationalization, in both spectral and physical spaces, is based on some inherent properties of forced quasi-geostrophic (QG) stratified turbulence, and on analytical arguments from the quasi-geostrophic equations. One novel aspect we focus on is the fully 3-D cascade of the density-compensated thermohaline anomalies by the mesoscale eddy field. That is, not only the horizontal cascade but also the vertical one is investigated. Other aspects include the rationalization of the mesoscale thermohaline anomalies based on potential vorticity arguments, and the location in physical space of the formation of the small-scale density-compensated thermohaline fronts relative to the eddy field.

In most of this study, we consider the situation of an idealized distribution of the large-scale forcings of the salinity and temperature fields: the isotherms are horizontal and the isohalines vertical. These large-scale anomalies are not unrealistic since similar characteristics can be encountered in the Northeast Atlantic at a depth of 1000 m, where a large-scale thermohaline front separates the Mediterranean Water from the Intermediate

Arctic Water (Arhan and King, 1995). However, the main argument for using such *orthogonal* large-scale temperature and salinity forcings is that they highlight the rôle of the dynamical processes driving the QG turbulence in the formation of strongly density-compensated, small-scale thermohaline fronts. Furthermore we use the approximation that the equation of state is linear. The next section explains the appearance of density-compensated, small-scale thermohaline fronts in a fully turbulent QG stratified flow, using the well-known properties of QG turbulence. Section 3 reports on some numerical results on the formation and spatial distribution of the thermohaline fronts, using the QG 3-D spectral model of Hua and Haidvogel (1986) (hereafter HH86). Sections 4 and 5 attempt to rationalize the horizontal and vertical cascade of the thermohaline anomalies, as well as the location of the thermohaline fronts in physical space.

2. QG stirring of temperature and salinity fields

We consider a QG stratified turbulent flow whose stratification is represented by the Brunt-Väisälä profile,

$$N^2(z) \equiv -\frac{g}{\rho_o}\frac{d\langle\rho\rangle}{dz}(z),$$

with g the acceleration of gravity, ρ_o and $\langle\rho\rangle$ respectively the constant and vertically varying part of the density field of the basic state. The QG turbulent flow is forced by the baroclinic instability of a mean vertically sheared zonal current, $\overline{U}(z)$, related to a large-scale meridional density gradient, $d\overline{\rho}/dy$ (with $\overline{\rho}$ the meridionally varying part of the density field of the basic state), through the thermal wind balance.

The density fluctuation is approximated as a linear combination of temperature (T) and salinity (S):

$$\rho = -\alpha T + \beta S, \tag{1}$$

with α and β the constant thermal and salinity expansion coefficients, respectively. For the sake of simplicity, and to be consistent with the density field of the basic state, the large-scale forcings of the temperature and salinity fields are chosen to be:

$$\beta\overline{S}(y, z) = \Gamma_S y - \frac{\rho_o}{g}\int N_S^2(z)\, dz, \tag{2}$$

$$-\alpha\overline{T}(y, z) = \Gamma_T y - \frac{\rho_o}{g}\int N_T^2(z)\, dz, \tag{3}$$

with:

$$\Gamma = \Gamma_S + \Gamma_T = \frac{d\overline{\rho}}{dy}, \quad N^2 = N_S^2 + N_T^2 = -\frac{g}{\rho_o}\frac{d\langle\rho\rangle}{dz}, \tag{4}$$

where Γ_S and Γ_T are constant.

a. Thermohaline anomalies in geostrophic turbulence

The time evolution of the salinity and temperature perturbations,[2] forced by the large-scale forcings (2) and (3), and advected by the QG turbulent flow, is given by:

$$\frac{d\beta S}{dt} + v\Gamma_S - w' \frac{\rho_o}{g} N_S^2 = 0, \tag{5}$$

$$\frac{d(-\alpha T)}{dt} + v\Gamma_T - w' \frac{\rho_o}{g} N_T^2 = 0, \tag{6}$$

where $d/dt = \partial/\partial t + (\overline{U} + u)\,\partial/\partial x + v(\partial/\partial y)$, with u, v respectively the zonal and meridional components of the geostrophic velocity associated with the mesoscale eddy field, and w' the ageostrophic vertical velocity.

From (1), the linear combination $\beta S - \alpha T$ leads to the density equation:

$$\frac{d\rho}{dt} + v\frac{d\overline{\rho}}{dy} + w'\frac{d\langle\rho\rangle}{dz} = 0. \tag{7}$$

However two linear combinations lead to different equations that help to understand the production and spatial distribution of the thermohaline anomalies. If we define $\tilde{\chi} \equiv N_T^2\beta S + N_S^2\alpha T$ and $\tilde{\gamma} \equiv \Gamma_T\beta S + \Gamma_S\alpha T$, we obtain the following equations:

$$\frac{d\tilde{\chi}}{dt} + v\Delta = 0, \tag{8}$$

$$\frac{d\tilde{\gamma}}{dt} + w'\frac{\rho_o}{g}\Delta = 0, \tag{9}$$

with $\Delta \equiv \Gamma_S N_T^2 - \Gamma_T N_S^2$. Let us assume $\Delta \neq 0$, which means that the isotherms and isohalines of the large-scale forcings depart from the isopycnals of the basic state. In that situation (7), (8) and (9) are the key equations to understand the production of density-compensated thermohaline fronts in geostrophic turbulence. Indeed, (8) is the equation of a tracer field which is forced by a large-scale field and horizontally advected by a geostrophic flow. From the properties of geostrophic turbulence (Rhines, 1983), such a forced tracer undergoes a direct horizontal cascade leading to a statistical equilibrium that is character-ized by a wavenumber spectrum with a spectrum slope between k^{-2} and k^{-1} (with k the horizontal wavenumber). The consequence is that the variance of the horizontal gradients of this tracer is mostly explained by the contribution of the smallest horizontal scales; i.e., the small-scale horizontal gradients are very energetic. On the other hand, the density

---

2. The equations introduced in this section are perturbations equations. This means that diffusive processes, omitted in the discussion for the sake of simplicity, only affect the perturbation fields and not the forcing fields.

perturbation of a forced-damped QG stratified turbulent flow field, and any forced tracer whose governing equation is similar to (7) [e.g. with analogous large-scale forcings], is known to be characterized by a very steep spectrum slope (between k^{-5} and k^{-6}) (cf HH86). Thus the density perturbation field is large scale and its small-scale horizontal gradients are very weak. The dynamical processes that lead to these important and very different properties of ρ and $\tilde{\chi}$ are further elaborated and discussed in the next section. Let us consider now Eq. (9). So far we know nothing (from the geostrophic turbulence studies) about the statistical properties of $\tilde{\gamma}$ that is a tracer forced by the vertical advection. However, if we consider the linear relation:

$$\rho = \frac{\Gamma \tilde{\chi} - N^2 \tilde{\gamma}}{\Delta} \tag{10}$$

(with N^2, Γ and Δ constant at a given level), we can deduce the statistical properties of $\tilde{\gamma}$: insofar as the variance of ρ and $(\Gamma/\Delta)\tilde{\chi}$ have the same order of magnitude, the tracer field $(N^2/\Delta)\tilde{\gamma}$ should be characterized by very energetic small-scale horizontal gradients that strongly compensate for the energetic small-scale horizontal gradients of $(\Gamma/\Delta)\tilde{\chi}$. In other words the spectrum of $\tilde{\gamma}$ should be characterized by a slope between k^{-2} and k^{-1} and its energetic small-scale features should be *strongly anticorrelated* with those of $\tilde{\chi}$.

The consequences of the strong difference between the properties of ρ and those of $\tilde{\chi}$ and $\tilde{\gamma}$, on the *T/S* anomalies and the thermohaline fronts, emerge from the two following linear relations:

$$\beta S = \frac{\Gamma_S \tilde{\chi} - N_S^2 \tilde{\gamma}}{\Delta}, \quad -\alpha T = \frac{\Gamma_T \tilde{\chi} - N_T^2 \tilde{\gamma}}{\Delta}. \tag{11}$$

Since $\Delta \neq 0$, these linear relations differ from (10). Consequently there is no exact compensation between the energetic small-scale features of $\tilde{\chi}$ and those of $\tilde{\gamma}$ for the *S* and *T*-fields. The consequence is that in a fully turbulent QG flow the salinity and temperature horizontal gradients should be energetic and, from (1), strongly density compensated.

b. Mechanisms involved in the density compensation of the thermohaline fronts

As shown above the appearance of small-scale density-compensated thermohaline fronts in a QG stratified turbulent flow can be explained using two important properties: the characteristics of the density field (ρ), that is entirely large scale, and those of a tracer field which is horizontally advected ($\tilde{\chi}$), that is dominated by small scales. In order to better understand the mechanisms involved in the formation of these density-compensated fronts, we consider now an idealized large-scale thermohaline distribution which highlights the role of the dynamical processes involved in (7) and (8): the large-scale forcings of salinity and temperature (defined by (2) to (4)) are chosen such that $\Gamma_T = N_S^2 = 0$ and $\Delta \neq 0$, i.e. the large-scale isotherms are purely horizontal while the large-scale isohalines are purely vertical. Then the variables χ and γ defined by $\chi \equiv (\Gamma_S/\Delta)\tilde{\chi}$ and $\gamma \equiv (N_T^2/\Delta)\tilde{\gamma}$ can be

directly associated to the density contributions of the salinity and temperature perturbations, respectively (i.e. $\chi = \beta S$ and $\gamma = -\alpha T$). Their equations are:

$$\frac{d\chi}{dt} + v\frac{d\overline{\chi}}{dy} = 0, \tag{12}$$

$$\frac{d\gamma}{dt} + w'\frac{d\overline{\gamma}}{dz} = 0, \tag{13}$$

with $d\overline{\chi}/dy = \Gamma_S$ and $d\overline{\gamma}/dz = -(\rho_o/g)N_T^2$. The properties of χ, ρ ($=\chi + \gamma$) and γ and the mechanisms involved in their time evolution can now be directly discussed within the context of the dynamical processes that drive the QG turbulence.

i. Properties of the χ-field. The equation for χ, similar to (8), is that of a tracer that is known to experience a direct horizontal cascade leading to the production of very energetic small-scale horizontal gradients (Rhines, 1983). This production is inferred from the equation for $\nabla\chi$ (with ∇ the horizontal gradient operator) which reads:

$$\frac{d\nabla(\chi + \overline{\chi})}{dt} = -\mathbf{A}\nabla(\chi + \overline{\chi}) \tag{14}$$

where $\mathbf{A}$ is a matrix defined as:

$$\mathbf{A} \equiv \frac{1}{2}\begin{bmatrix} \sigma_n & \sigma_s + \omega \\ \sigma_s - \omega & -\sigma_n \end{bmatrix}, \tag{15}$$

ω, σ_n and σ_s are respectively the vorticity and the normal and shear strain rates defined as: $\omega \equiv \partial v/\partial x - \partial u/\partial y$, $\sigma_n \equiv \partial u/\partial x - \partial v/\partial y$ and $\sigma_s \equiv \partial v/\partial x + \partial u/\partial y$. Note that $\mathbf{A}$ is just the transpose of $\mathbf{A^*} = \nabla\mathbf{U}$, the velocity gradient tensor. Its eigenvalues are $\pm\lambda_0^{1/2}$ where:

$$\lambda_0 = \frac{1}{4}[\sigma_n^2 + \sigma_s^2 - \omega^2]. \tag{16}$$

The quantity λ_0 has been derived by Okubo (1970) and later on by Weiss (1991), and used to partition the fluid into regions with different dynamical properties from the point of view of tracer gradient evolution. Indeed, using the assumption that the velocity gradients are slowly varying along a Lagrangian trajectory, the behavior of the tracer gradient can be said to be locally determined by the nature of the eigenvalues of $\mathbf{A}$. It follows that the horizontal χ-gradients cannot grow in vortex cores where $\lambda_0 < 0$ since the eigenvalues of $\mathbf{A}$ are purely imaginary. On the other hand, in strain-dominated areas where $\lambda_0 > 0$, the eigenvalues of $\mathbf{A}$ are real and the horizontal χ-gradients can exponentially grow. This growth can be very rapid since the time scale involved in the eigenvalues of $\mathbf{A}$ is statistically linked to that of the enstrophy (Hua, 1994), i.e. a very short time scale compared to the advective time scale. Thus the χ-fronts should grow very rapidly in strain-dominated areas.

ii. Properties of the ρ-field. In stratified QG turbulence, the density field is known to be characterized by quite weak small-scale horizontal gradients (cf HH86). The key to physically understand this very important property, and in particular the mechanisms that strongly inhibit the formation of density gradients, is to consider the role of the ageostrophic circulation in maintaining the thermal wind balance (Hoskins *et al.,* 1978). Let us briefly comment on this point. The thermal wind balance, that results from the geostrophic and hydrostatic equilibria of the velocity and pressure field at zeroth order (in Rossby number), reads:

$$\nabla(\rho + \overline{\rho}) = \mathbf{k} \times \frac{f_0 \rho_0}{g} \frac{\partial \mathbf{u}}{\partial z} \tag{17}$$

with $\mathbf{k}$ the vertical unit vector, $\mathbf{u} = (u + \overline{U}, v)$ and f_o the Coriolis parameter (using the f-plane approximation for the sake of simplicity).

From the momentum and density equations for a QG flow, the equations for the two parts of the thermal wind balance read:

$$\frac{d\nabla(\rho + \overline{\rho})}{dt} = -\mathbf{A}\nabla(\rho + \overline{\rho}) + \frac{N^2 \rho_o}{g} \nabla w' \tag{18}$$

$$\frac{d}{dt}\left[\mathbf{k} \times \frac{f_o \rho_o}{g} \frac{\partial \mathbf{u}}{\partial z}\right] = \mathbf{A}\left[\mathbf{k} \times \frac{f_o \rho_o}{g} \frac{\partial \mathbf{u}}{\partial z}\right] + \frac{\rho_o}{g} \frac{\partial}{\partial z} [\mathbf{u}' - \mathbf{k} \times f_o\nabla p'] \tag{19}$$

with $\mathbf{u}' = (u', v')$ the ageostrophic horizontal velocity component and p' the ageostrophic velocity. The matrix $\mathbf{A}$ (defined by (15)) appears in (18) and *with the opposite sign* in (19). Consequently, in areas where the eigenvalues of $\mathbf{A}$ are real ($\lambda_0 > 0$) like in strain dominated areas, the nonlinear geostrophic term involving $\mathbf{A}$ will induce an exponential growth of horizontal density gradients and an exponential decay of the corresponding vertical gradients of the horizontal velocity, leading to a rapid destruction of the thermal wind balance. This thermal wind *imbalance* created by the nonlinear geostrophic terms causes motions to depart from geostrophy and thus induces an ageostrophic circulation. In the QG approximation the role of this ageostrophic circulation (through the second terms on the right-hand sides of (18) and (19)) is to instantaneously reestablish geostrophy. In other words the thermal wind balance is destroyed by the nonlinear geostrophic dynamics but is instantaneously restored by the ageostrophic circulation. This is how the ageostrophic circulation prevents the formation of strong horizontal density gradients and vertical gradients of the horizontal velocity: this leads to a steep spectrum slope (between k^{-5} and k^{-6}) of the density field, and therefore of the $\chi + \gamma$-field.

iii. Properties of the γ-field. From the arguments developed in Section 2a, these quite different statistical properties of the $\chi + \gamma$ and χ-fields lead us to deduce (insofar as the variance of $\chi + \gamma$ and χ have the same order of magnitude) that the γ-field, which is forced only by the vertical advection, should be characterized by energetic small-scale horizontal gradients that are *strongly anticorrelated* with the energetic small-scale horizontal gradi-

ents of χ. It follows, from the preceding discussion on the mechanisms that drive the evolution of the perturbated density field and its characteristics, that this strong anticorrelation between the small-scale horizontal gradients of χ and γ can be explained by the existence of a relationship that involves the ageostrophic vertical velocity, the Okubo-Weiss quantity λ_0 and the horizontal and vertical forcings of the density field. Since λ_0 is directly related to the Laplacian of the ageostrophic pressure (see Hua *et al.,* 1998), one can say that the ageostrophic circulation is the key dynamical characteristics that governs the strength and the spatial distribution of these thermohaline fronts.

3. Numerical simulations

The formation and spatial distribution of the thermohaline fronts have been assessed through direct numerical simulations of the advection of the salinity and temperature density contributions by a forced-damped QG stratified turbulent flow on the β-plane. The forcing mechanism is provided by the baroclinic instability of a vertically sheared flow $\overline{U}(z)$. Damping is produced by a bottom Ekman layer (at $z = -H$) and parameterized with a friction coefficient κ. The simulations make use of the 3-D spectral model described in HH86 to integrate the following equation for the perturbated potential vorticity (q):

$$\frac{dq}{dt} + v\frac{\partial \overline{q}}{\partial y} = -\kappa\Delta\varphi\big|_{z=-H,} \tag{20}$$

with φ the streamfunction and where

$$q = \Delta\varphi + \partial/\partial z(f_o^2 N^{-2}\partial\varphi/\partial z)$$

and

$$\partial\overline{q}/\partial y = \beta - \partial/\partial z(f_o^2 N^{-2}\,\partial\overline{U}/\partial z)$$

In addition, $f = f_o + \beta y$ is the Coriolis parameter and $N^2(z)$ an exponential Brunt-Väisälä profile. Physical parameters are the same as those used in the pivot simulation of HH86 except for the friction coefficient that is three times smaller (see Table 1 in HH86). Hyperviscosity is used to remove enstrophy at the smallest scales. Nondimensionalization, using an appropriate velocity scale and a length scale that is the domain size, is such that the nondimensional time unit corresponds to an advective time scale of 34 days. The first Rossby radius of deformation (whose dimensional value is 50 km) corresponds to the nondimensional wavenumber $k_R = 7$. Thus the corresponding dimensional length of the domain size is $L \approx 2000$ km. The numerical resolution involves 256×256 Fourier modes on the horizontal. A normal mode expansion has been used on the vertical that leads to approximate the streamfunction, φ, by the following truncated series:

$$\varphi(x, y, z, t) = \sum_{m=0}^{M} \varphi_m(x, y, t)F_m(z), \tag{21}$$

where F_m are the eigenmodes of the Sturm-Liouville problem involving $N^2(z)$. The numerical resolution involves eight vertical normal modes ($M = 8$).

The large-scale thermohaline forcings used in the numerical simulations are those involved in the idealized large-scale thermohaline situation of Section 2b: the salinity density contribution (χ) is forced by $\partial \overline{\rho}/\partial y$ ($= \partial \overline{U}/\partial z$) and the temperature density contribution (γ) is forced by $d|\rho|/dz$ ($= -(f_o^2/g)N^2(z)$). As in HH86, $d|\rho|/dz(z)$ has an exponential vertical profile with a maximum near the surface and the vertical profile of $\partial \overline{\rho}/\partial y(z)$ is that of the first baroclinic mode with a maximum near 500 m. Within the quasi-geostrophic approximation, the z-dependence of $\partial \overline{\rho}/\partial y$ has no impact on the equation for χ. Thus the large-scale isohalines are almost vertical and the large-scale isotherms are purely horizontal. The integration of Eqs. (12) and (13) for χ and γ is similar to that of the potential vorticity equation but using an appropriate vertical modes representation. Their integration makes use of the horizontal geostrophic velocity components deduced from the streamfunction field and of the ageostrophic vertical velocity obtained from the equation for the density ($\rho = -\partial \varphi/\partial z$). Note that ρ, χ and γ are nondimensional variables with the characteristics density scale being $\rho_o \varepsilon F$ (with ε the Rossby number and $F \equiv f_o^2 L^2/gH$). Initial conditions for $\chi + \gamma$ and ρ are identical and the numerical simulations performed have clearly confirmed that both fields remain identical at any depth. The next two subsections examine the characteristics of χ and γ (the salinity and temperature density contributions, respectively) and their differences with the density field.

a. Fields of T/S anomalies and of density

A statistical analysis performed at different times reveals that the variances of ρ, χ and γ, at any depth between 100 m and 1200 m, have the same order of magnitude and their spectra (not shown) exhibit a peak near the wavenumber $k = 4$. However their spectrum slopes strongly differ: the ones of χ and γ are close to k^{-2} whereas the one of ρ is close to k^{-6}.

Figures 2a, b and c show the fields of ρ, χ and γ at a depth of 800 m after an integration time of 30 time units. Note that positive values of χ and γ refer respectively to salty and cold water and negative values to fresh and warm water because of the particular large-scale thermohaline forcings that have been chosen. The contour intervals on these figures are identical in order to better reveal the differences in terms of horizontal gradients. Since density is mainly captured by the first baroclinic mode, its isolines are close to the streamlines (with the opposite sign) and as such, identify well the location of the mesoscale eddy cores which roughly correspond to the extrema of ρ. The ρ-field (Fig. 2a) is mostly dominated by mesoscale structures and displays rather weak horizontal gradients. Analysis of Figures 2a, b and c reveals that, within the eddies core, the positive contribution to ρ mainly comes from χ whereas γ has mostly a negative impact. Thus in terms of thermohaline anomalies the cores of the cyclonic eddies, which are denser, are salty and warm whereas the cores of the anticyclonic eddies, which are lighter, are fresh and cold. The χ and γ-fields (Figs. 2b and 2c) are characterized by the presence of energetic
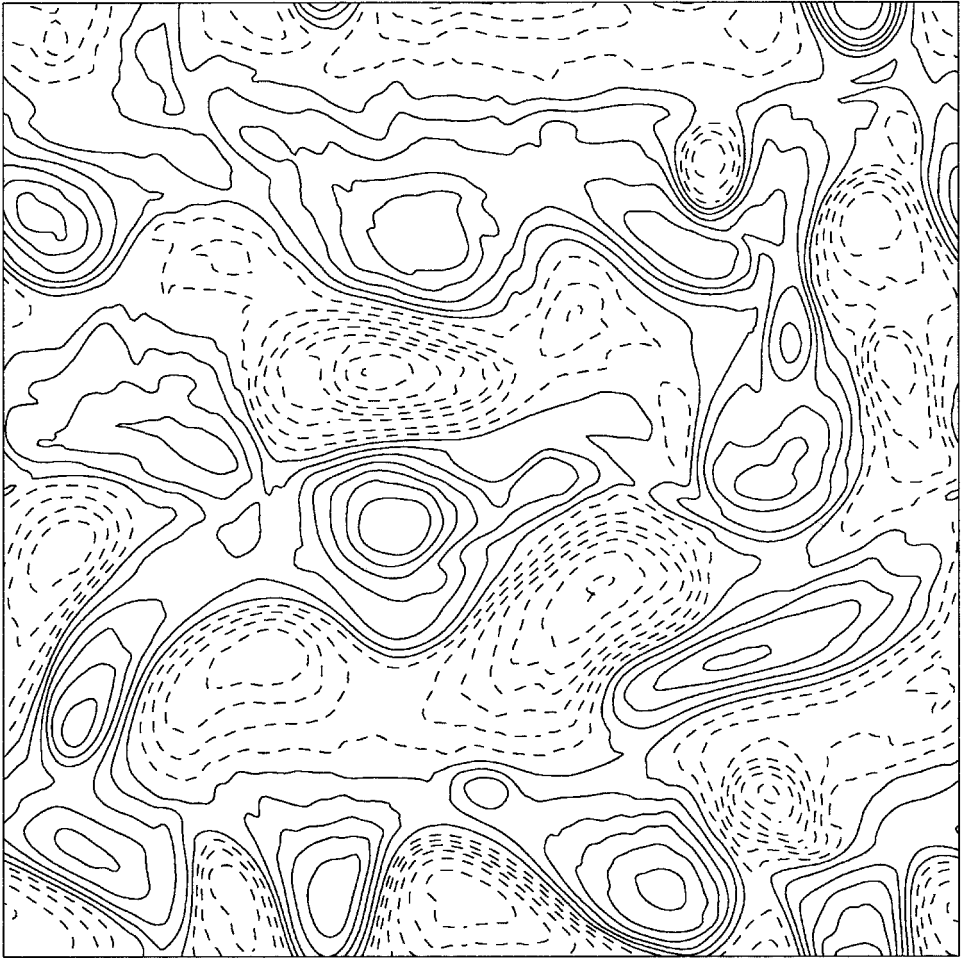
Density at z= 800

Figure 2. Isocontours of the horizontal fields of ρ (a), χ (b) and γ (c) at a depth of 800 m. The dimensional length of the domain is $L = 2000$ km. The contour interval in nondimensional units is 1 for the three fields. The isocontours range from -14 to 14 for χ, from -11 to 13 for γ and from -8 to 6 for ρ. Solid and dashed lines respectively refer to positive and negative values.

small-scale structures that have the form of elongated tongues and filaments of either warm and salty or cold and fresh water. These small-scale structures of the χ and γ-fields are strongly anticorrelated since they are absent in the ρ-field (Fig. 2a) that is identical to $\chi + \gamma$-field.

Figure 3 shows the spatial distribution of the χ-horizontal gradients whose values are larger than the nondimensional value of 100. These gradients have locally a value ten times larger than that of the corresponding density gradients. Thus they are strongly compensated by the energetic horizontal gradients of γ and consequently are strongly anticorrelated with

X at z= 800.0m

Figure 2. (Continued)

those gradients. These strongly anticorrelated χ and γ-horizontal gradients are what we call the thermohaline fronts. They involve thin filaments and are characterized by small horizontal scales. Most of the χ-fronts are almost aligned with the density isocontours. But some of them cross the density isocontours (Fig. 3). The latter thus have no signature on the density field.

The examination of the vertical spatial distribution of χ or γ relative to the density field reveals some interesting features related to the *T/S* anomalies. Figures 4a and 4b show vertical sections of the ρ and χ-field. The vertical section of the ρ-field displays mesoscale features with a maximum near 500 m. These features have a low vertical mode structure close to the first baroclinic mode. On the other hand, the vertical section of the χ-field displays quite small horizontal, as well as, small vertical energetic structures that are absent

Υ at z= 800

Figure 2. (Continued)

in the ρ-field. These small-scale vertical features that are distributed over a depth up to 1500 m (Fig. 4b) clearly reveal that the small-scale horizontal thermohaline anomalies and the associated energetic thermohaline fronts are characterized by small vertical scales.

Thus the numerical results clearly illustrate that the thermohaline anomalies are strongly anticorrelated, strongly density compensated and are characterized by small horizontal and vertical scales.

b. Relation between the thermohaline anomalies and the potential vorticity

Equation for χ (12) differs from the one for the potential vorticity q (20) only through the forcing term and the bottom friction term. So the only difference between χ and q in the

$$|\nabla \mathcal{X}| \text{ at } z= \ \ 800.0\text{m}$$

Figure 3. Horizontal χ-gradients at the same level and time as Figure 2. Dark areas correspond to the highest values of $|\nabla \chi|$ (from 100 up to 500 in nondimensional units). Isocontours of the perturbated density are shown.

upper layers is the forcing term. This means that, insofar as the initial conditions are quite close, we should expect in these layers the χ-field to resemble the potential vorticity field at any depth through the relation:

$$\chi \approx q \, \frac{\dfrac{\partial \overline{\rho}}{\partial y}(z)}{\dfrac{\partial \overline{q}}{\partial y}(z)}. \tag{22}$$

$$\rho$$
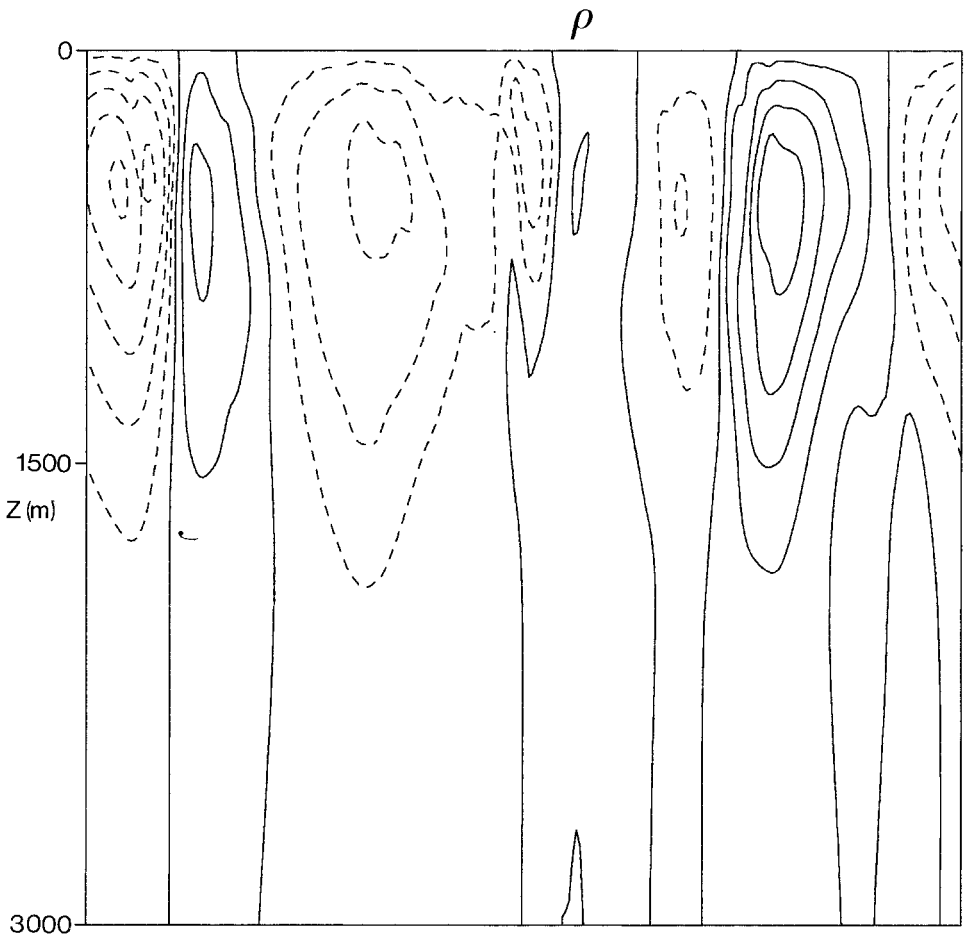

Figure 4. Vertical sections of ρ (a) and χ (b) at the same time as Figure 2. The contour interval in nondimensional units is 1 for both fields. The isocontours range from −8 to 6 for ρ and from −14 to 14 for χ. Solid and dashed lines respectively refer to positive and negative values.

Figure 5 shows the correlation between the χ and q-horizontal fields at different depths. Although the initial conditions used for χ and q in the simulations performed are not quite similar, the numerical results display a correlation larger than 0.9 between 100 m and 1000 m. This correlation changes its sign at 2000 m and attains −0.8 at 2500 m. At depth larger than 3500 m the correlation becomes weak (≈ -0.2). The sign change at 2000 m is due to $\partial \bar{q}/\partial y$ that is positive above 2000 m and negative below while $\partial \bar{p}/\partial y$ is positive throughout the water column. The weak correlation below 3500 m is due to the influence of the bottom Ekman friction that affects q and not χ. The strong similarity between the χ and q-horizontal fields in the upper layers is illustrated by the comparison between Figure 2b and Figure 6 that reveals the almost perfect overlap in physical space of the mesoscale as
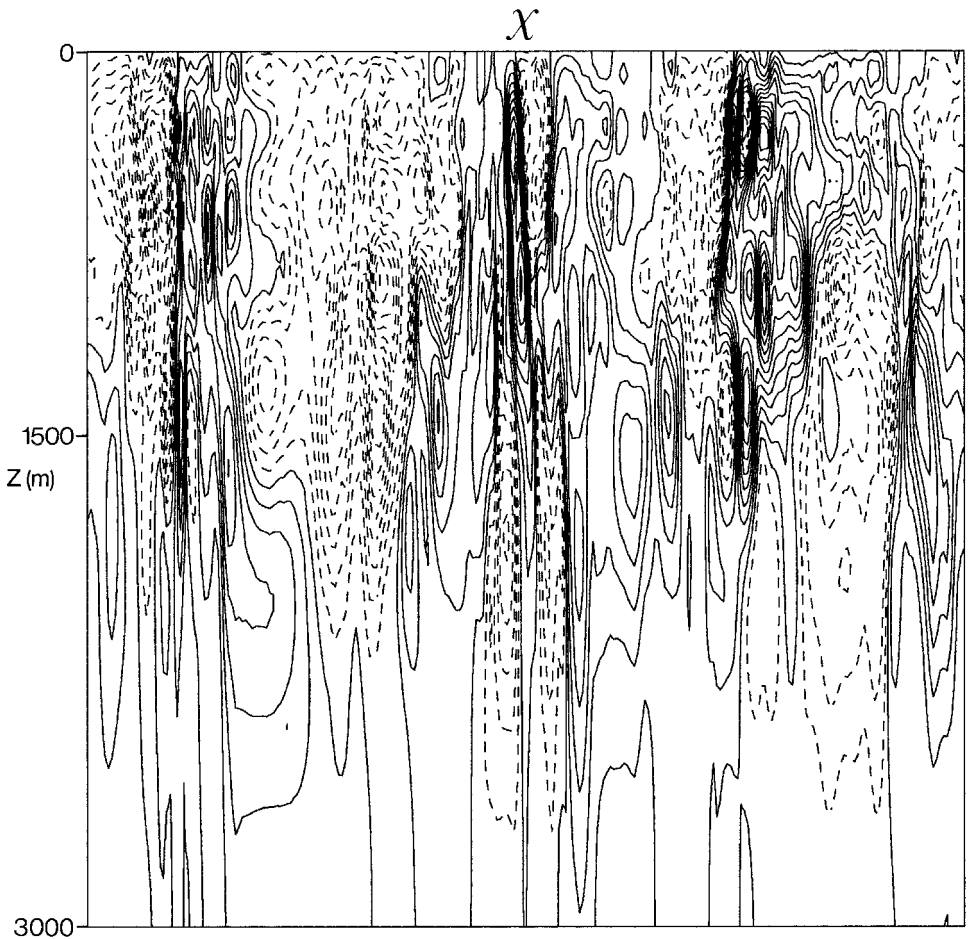
$$\chi$$

Figure 4. (Continued)

well as the small-scale features of both fields. One important consequence is that most of the thermohaline fronts are potential vorticity fronts.

The strong correlation between the χ and q-horizontal fields in the upper layers allows us to understand the order of magnitude of the mesoscale anomalies of salinity and temperature (in terms of χ and γ contributions) relatively to the density itself. Let us consider an eddy core characterized by a horizontal wavenumber K such that:

$$\beta / \overline{U} < 2K^2 < k_R^2. \qquad (23)$$

This relation is reasonable in the upper layers for a forced quasi-geostrophic stratified turbulent flow since the most energetic length scales (K^{-1}, with $K = 4$ in our simulations) are usually larger than the first Rossby radius of deformation (k_R^{-1}) and smaller than the Rhines scale (HH86). Furthermore let us assume that the eddy core is mainly captured by
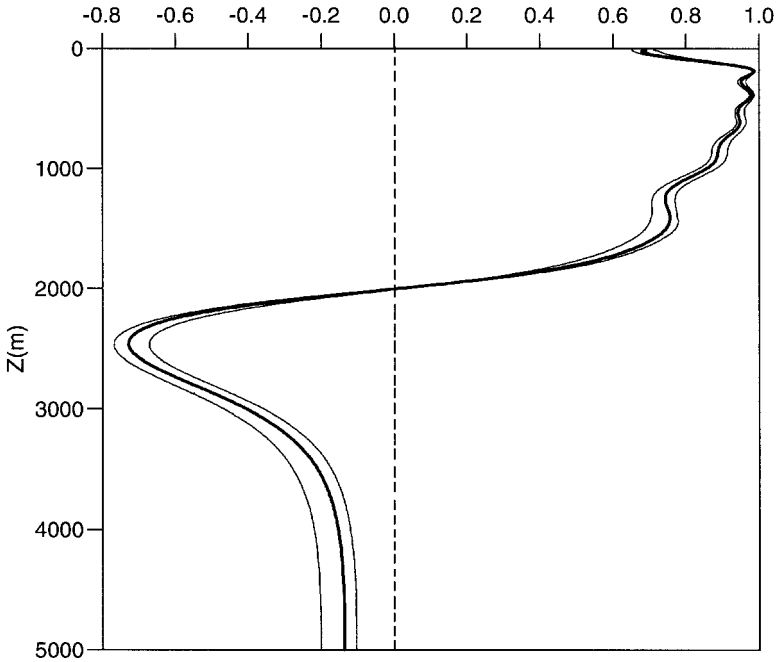
Figure 5. Vertical profile of the correlation between χ and q. The thick line represents the values averaged over a period of a year while the thin lines represent the extrema over this period.

the first two vertical modes (the barotropic and the first baroclinic ones) whose order of magnitude are found to be almost equal in the upper layers. Then, from (22) and using $\partial \overline{q}/\partial y = [\beta + k_R^2 \overline{U}]$ and the expressions for q and ρ in terms of the barotropic and the first baroclinic modes, we get:

$$\chi \approx \frac{2K^2 + k_R^2}{\dfrac{\beta}{\overline{U}} + k_R^2} \rho \tag{24}$$

$$\gamma \approx \frac{\dfrac{\beta}{\overline{U}} - 2K^2}{\dfrac{\beta}{\overline{U}} + k_R^2} \rho. \tag{25}$$

These relations reveal that within the eddies that verify (23), χ and ρ have the same sign while γ and ρ have different signs. Furthermore they show that the orders of magnitude of the three quantities χ, γ and ρ are similar, which rationalizes the numerical results of the preceding section. At last, since χ is related to the salinity and γ to the temperature because of the chosen large-scale thermohaline forcings, this explains why the cyclonic eddies that
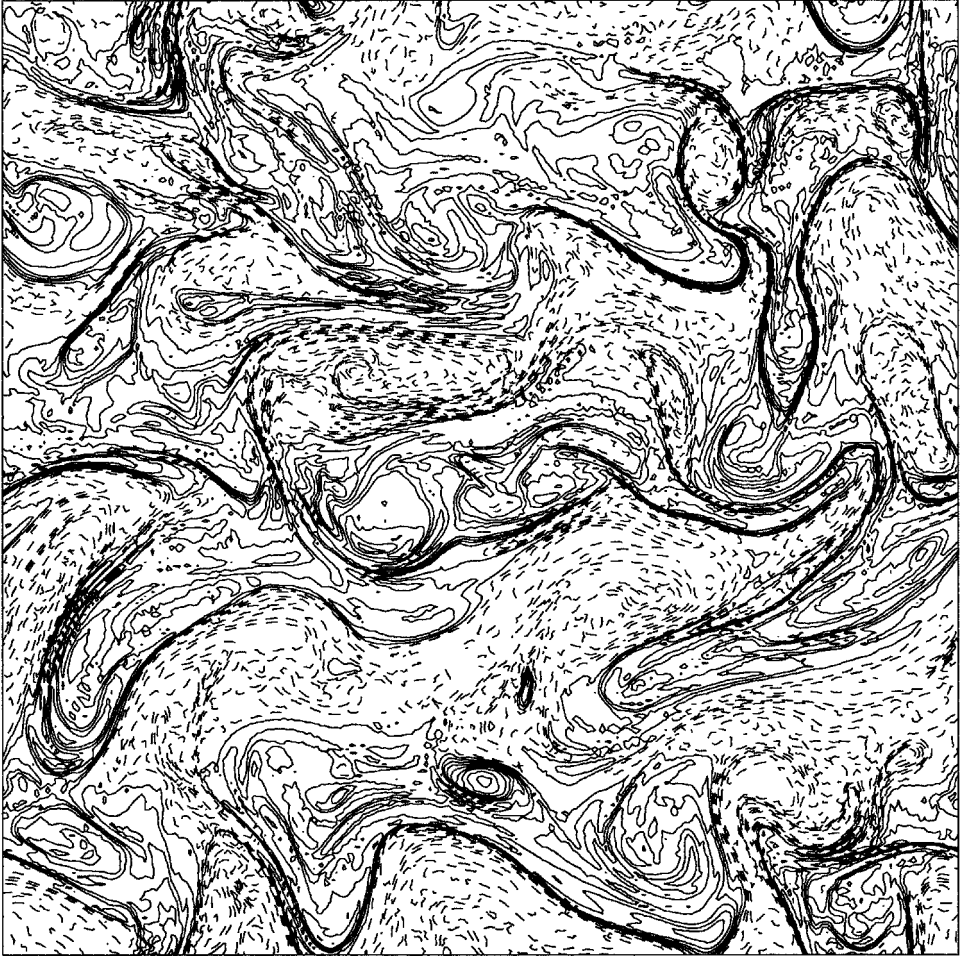
Potential Vorticity   at z= 800.0m

Figure 6. Potential vorticity field at the same level and time as Figure 2. The contour interval in nondimensional units is 10 and the isocontours range from −80 to 90. Solid and dashed lines respectively refer to positive and negative values.

are denser are salty and warm, whereas the anticyclonic eddies that are lighter are fresh and cold.

c. Evidence of a three-dimensional cascade of the thermohaline fronts

To measure quantitatively the difference between the thermohaline fronts and the density fronts we have calculated at different depths $|\overline{\nabla\chi}|$ and $|\overline{\nabla\rho}|$ where:

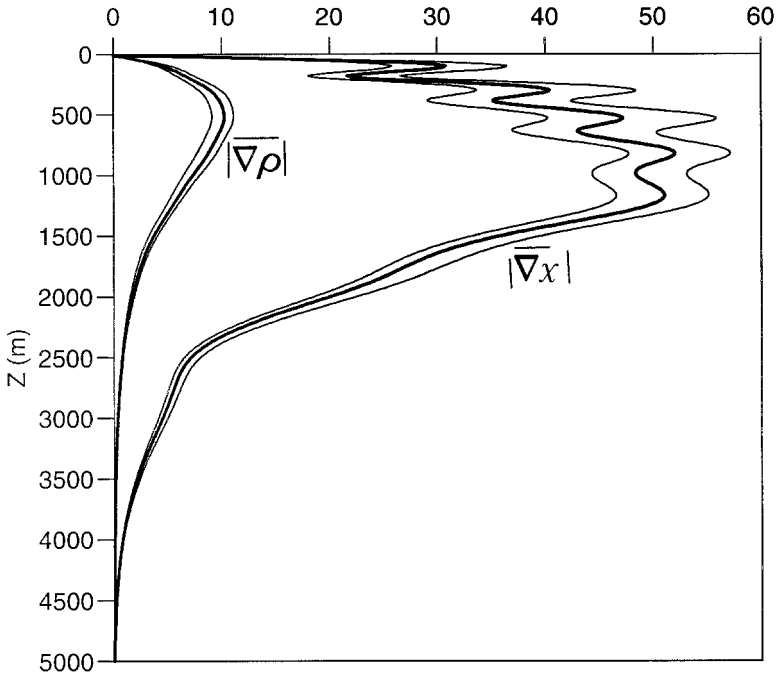$$|\overline{\nabla X}| = \frac{1}{\mathscr{A}} \iint_{\mathscr{A}} [\nabla^* X \nabla X]^{1/2} \, dxdy \tag{26}$$

Figure 7. Vertical profiles of $|\overline{\nabla\rho}|$ and $|\overline{\nabla\chi}|$ in nondimensional units. The thick lines represent the values averaged over a period of a year while the thin lines represent the extrema over this period.

with $\mathscr{A}$ the horizontal domain and X either χ or ρ. Again ∇ designates the horizontal gradient operator and $*$ the transpose. These quantities have been calculated at different times over a period of a year (≈ 10 time units).

The corresponding vertical profiles (Fig. 7) first reveal that the time dispersion of $|\overline{\nabla\rho}|$ and $|\overline{\nabla\chi}|$ is less than 20% of the mean value at any depth. Values of $|\overline{\nabla\chi}|$ in the first 1200 m are much larger than the maximum values of $|\overline{\nabla\rho}|$: their ratio is 4.5 at 500 m (where $|\overline{\nabla\rho}|$ is maximum) and increases up to 8 at 1200 m (where $|\overline{\nabla\chi}|$ attains one of its largest values). Since the horizontal spectrum of χ has a k^{-2} slope in the first 1200 m, the large values of $|\overline{\nabla\chi}|$ at these depths are mostly explained by the contribution of the smallest horizontal scales. In other words the large values of $|\overline{\nabla\chi}|$ are mainly explained by the most intense χ-fronts as the ones shown in Figure 3. On the other hand the small horizontal scales of ρ very weakly contribute to $|\overline{\nabla\rho}|$ because of the steep ($\approx k^{-6}$) spectrum slope of the density. This quantitative analysis confirms that the thermohaline anomalies experience a significant 2-D horizontal cascade whereas the density *does not,* which leads to intense thermohaline gradients strongly density compensated.

The last comment concerns the vertical distribution of these horizontal gradients. $|\overline{\nabla\rho}|$ is maximum at 500 m and then exponentially decays with increasing depths. A rationalization of this result comes from an analysis, in terms of baroclinic mode contribution, that has revealed that $|\overline{\nabla\rho}|$ is mostly captured (as that of ρ) by the first baroclinic mode which

exhibits only one maximum at 500 m. On the other hand the $|\overline{\nabla\chi}|$-profile displays a more complex vertical structure: Figure 7 reveals in the first 1200 m several well-defined maxima with a vertical spacing between 200 m and 400 m. Furthermore the largest maxima are located at deeper levels than the $|\overline{\nabla\rho}|$ maximum. The analysis in terms of vertical modes content reveals that the complex vertical structure of $|\overline{\nabla\chi}|$ is due to modes two to four. Since the forcing of χ ($\partial\overline{\rho}/\partial y(z)$) has a vertical structure that involves only the mode one, this implies that this tracer, besides the horizontal cascade, experiences as well a significant vertical cascade. Furthermore, since the density does not experience such a 3-D cascade and since $\rho = \chi + \gamma$, it can be stated that both the χ and γ-fields undergo a significant 3-D cascade. One consequence of this 3-D cascade of the thermohaline anomalies is that the ultimate mixing will not be necessarily maximum where the large-scale *T/S* forcings are maximum.

4. Topology of the 3-D cascade

A first insight into the rationalization of the strong horizontal and vertical cascades revealed in the preceding sections can be gained from the examination of the first order equation for the time evolution of the tracer gradients.

The results of Section 2b can be used to understand the 2-D horizontal cascade of the thermohaline anomalies and in particular the formation of strong horizontal gradients at a given depth. Indeed the examination of the first order equation (14) and the assumption of slowly varying velocity gradients along a Lagrangian trajectory led us to use the Okubo-Weiss quantity, λ_0, as a criterion to discriminate the regions of physical space where the horizontal cascade is strongly active (involving the largest positive λ_0-values) from those where the horizontal cascade is inhibited (involving the largest negative λ_0-values). Thus the spatial distribution of λ_0 should allow to identify the location of the thermohaline fronts relatively to the eddy field and to quantify their growth. Figure 8a shows the regions with large positive λ_0-values. These regions are mainly located in saddle areas and between co-rotating eddies, thus explaining the presence of thermohaline fronts in those regions of the flow (see Fig. 3).

The mechanisms that govern the vertical cascade and therefore the production of small vertical scales can be identified using an approach similar to the one followed by Haynes and Anglade (1997). Defining $k_h = (\chi + \overline{\chi})^{-1}\nabla(\chi + \overline{\chi})$ and $k_z = (\chi + \overline{\chi})^{-1}\partial(\chi + \overline{\chi})/\partial z$, and using $d(\chi + \overline{\chi})dt = 0$ we get:

$$\frac{dk_h}{dt} = -Ak_h, \qquad (27)$$
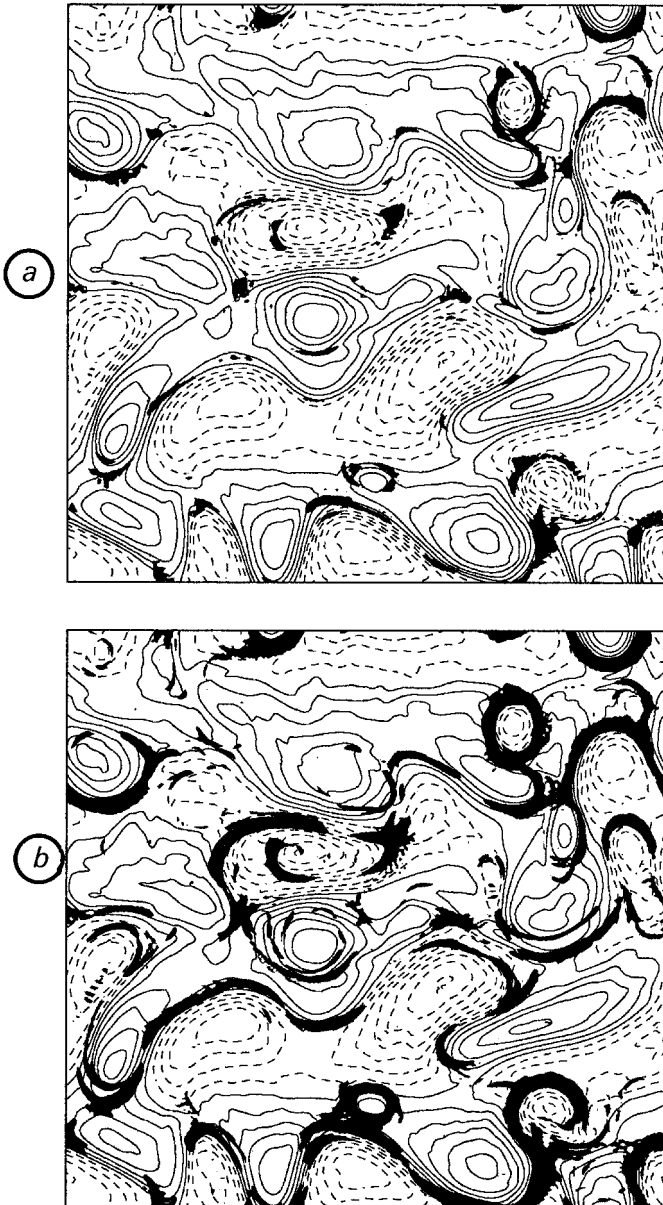
$$\frac{dk_z}{dt} = -Sk_h, \qquad (28)$$

Figure 8. Spatial distribution of λ_0 (a) and λ_+ (b) at the same level and time as Figures 2 and 3. Black areas correspond to the largest values (>100). Isocontours of the perturbated density are shown.

with $S = [\partial(u + \overline{U})/\partial z \, , \, \partial v/\partial z]$. These equations emphasize that the time evolution of k_h does not depend explicitly on k_z whereas the k_z-evolution entirely depends on k_h. Thus the vertical cascade is strongly constrained by (or "slaved" to) the horizontal cascade, through the action of the vertical shear of the horizontal velocity. Further insights into the 3-D

cascade can be obtained from the analytical expression of the aspect ratio of the thermohaline fronts, α, defined by $k_z = \alpha k_h$. Using (27) and (28), the equation for α is:

$$\frac{d\alpha}{dt} = \alpha A - S. \tag{29}$$

The matrix A appears in (27) and (29) but with the opposite sign. This means that, in the direction where the horizontal gradients grow, the aspect ratio α should tend to a steady solution. The exact form of the steady solution for α is (using $A^2 = \lambda_0 I$ with I the identity matrix):

$$\alpha = \frac{SA}{\lambda_0} = \left[-\frac{Q_2}{\lambda_0}, \frac{Q_1}{\lambda_0} \right] \tag{30}$$

where Q_1 and Q_2 are directly related to the components of the $\mathbf{Q}$-vector of Hoskins $et\ al.$ (1978). The $\mathbf{Q}$-vector is simply defined as being the nonlinear geostrophic terms that appear in the right-hand side of (18) and its divergence is equal to the 3-D normalized Laplacian of the ageostrophic vertical velocity (see Hoskins $et\ al.,$ 1978). Two comments arise from (30). First, since the $\mathbf{Q}$-vector and λ_0 are directly related to the ageostrophic circulation, it emphasizes the important rôle of the ageostrophic circulation in the 3-D cascade of the thermohaline fronts. Second, from the thermal wind relations, the density horizontal gradients are directly involved in the components Q_1 and Q_2. This means that the vertical wavenumber k_z can become large only in regions where both λ_0 and the density gradients are large. We have found that in those regions the ratio $|\alpha|$ is usually of order one (in nondimensional units). Thus in the black regions of Figure 8a, the results reveal that $|\alpha|$ ranges from 1.5 to 4.

5. A more accurate criterion for horizontal stirring properties

The preceding analytical arguments clearly show that the vertical cascade is strongly constrained by the horizontal one, which emphasizes the importance of the mechanisms that drive the formation of the horizontal gradients. As stated before, the use of λ_0 as a criterion to partition the horizontal physical space into regions of different dynamical properties is based on the assumption of a slowly varying velocity field. However the validity of this assumption has been questioned recently by Basdevant and Philipovitch (1994) and Hua and Klein (1998). To illustrate this point, let us consider the second order equation for the time evolution of the horizontal tracer gradient. From (14) we get:

$$\frac{d^2 \nabla(\chi + \overline{\chi})}{dt^2} = \left[A^2 - \frac{dA}{dt} \right] \nabla(\chi + \overline{\chi}) \tag{31}$$

where $A^2 = \lambda_0 I$. If the assumption of a slowly varying velocity field along a Lagrangian trajectory is valid, dA/dt should be negligible compared to A^2 and the eigenvalues of $A^2 - dA/dt$ should be just close to λ_0. However Basdevant and Philipovitch (1994) and Hua and Klein (1998) have found that the eigenvalues of dA/dt (denoted as $\pm\lambda_1$) can in some

regions be quite large when compared to λ_0, implying that the preceding assumption is not verified everywhere. In this context a new criterion for both particle dispersion and tracer gradient evolution, based on the acceleration gradient tensor, has been recently derived (Hua and Klein, 1998). The latter comes from considering the eigenvalues of the second order problem ($\lambda_\pm = \lambda_0 \pm \lambda_1$), and as such differs markedly from the Okubo-Weiss criterion. The distribution of λ_+ is shown on Figure 8b. We have found that the positive values of λ_+ and λ_0 are close in many regions such as saddle areas and between corotating eddies. However in other regions, in particular at the periphery of the eddies, λ_+ and λ_0 differ significantly: the ratio λ_+/λ_0 attains 2 to 3, thereby invalidating the assumption of slowly varying velocity field in those specific regions. The comparison of Figures 3 and 8b reveals that the majority of the thermohaline fronts are located in regions where λ_+ is the largest. This means that this criterion is more accurate in locating precisely the regions where tracer gradients are able to grow. The rationalization for using λ_+ instead of λ_0 as a criterion to identify the location of the formation of tracer gradients and to quantify their growth is detailed in Hua and Klein (1998) and Hua *et al.* (1998). As stated in Hua *et al.* (1998), the physical significance of using λ_+, i.e. of considering the second order problem instead of the first order one, can be explained as follows. Except in some sparse locations, the matrix A is not constant along a Lagrangian trajectory. In that sense the Okubo-Weiss criterion measures the growth associated with the instantaneous Eulerian strain rate rather than the strain rate averaged along a trajectory. So it is correct near the stagnation points (as in saddle areas) but it is misleading elsewhere. The second order problem, which leads us to use λ_+, takes into account this tendency. So it is like incorporating some trajectory averaging (over short trajectories). This explains why the use of λ_+ allows us to better identify the location of the thermohaline fronts in physical space.

6. Conclusion

We have investigated the stirring of the thermohaline anomalies in a fully turbulent time evolving stratified flow using idealized large-scale thermohaline forcings. The key assumption used is the quasi-geostrophic approximation verifies within the ocean interior. It allows us to rationalize the time evolution and the characteristics of the thermohaline anomalies in terms of some generic properties of forced QG turbulence, and in particular those of the density and potential vorticity fields which are characterized by very different spatial scales. This leads us to identify the 3-D ageostrophic circulation as the key dynamical process that governs both the strong density compensation of the small-scale thermohaline fronts and their spatial distribution relative to the eddy field. The numerical results illustrate the formation, by a mesoscale eddy field, of sharp thermohaline fronts with almost no signature on the density field. These fronts are mainly located in the saddle regions and around the eddy cores. Compared with the density fronts, their strength can be ten times larger. One novel aspect revealed by these numerical results is the efficient vertical cascade, strongly coupled to the horizontal one, that is experienced by the thermohaline anomalies. Another aspect concerns the location, in physical space, of the

formation of the small-scale density compensated thermohaline fronts relatively to the eddy field.

The experimental data often reveal that salinity and temperature can have a complex vertical distribution which is characterized by laminated structures, with a thickness of one or two hundreds meters and a strongly intermittent or filamentary horizontal structure (see for example Park *et al.,* 1997) which resemble some results of this study. So the following question arises: can the 3-D cascade of the thermohaline anomalies induced by the mesoscale eddy field be an alternating mechanism to explain the observed laminated structures, or interleaving phenomena, instead of the double diffusion mechanism often invoked in the litterature? Answering this question requires the systematic exploration of the 3-D cascade of the thermohaline anomalies and more specifically the vertical dimension. That necessitates, in particular, the consideration of a higher vertical resolution than the one considered in this study. We intend to explore this aspect in a future study.

REFERENCES

Arhan, M. 1990. The North Atlantic Current and Subartic Intermediate Water. J. Mar. Res., *48,* 109–144.

Arhan, M. and B. King. 1995. Lateral mixing of the Mediterranean Water in the eastern North Atlantic. J. Mar. Res., *53,* 865–895.

Basdevant, C. and T. Philipovitch. 1994. On the validity of the "Weiss criterion" in two-dimensional turbulence. Physica D, *73,* 17–30.

Chen, L. and W. R. Young. 1995. Density compensated thermohaline gradients and diapycnal fluxes in the mixed layer. J. Phys. Oceanogr., *25,* 3064–3075.

Haynes, P. and J. Anglade. 1997. Vertical cascade in tracer fields. J. Atmos. Sci., *54,* 1121–1136.

Hoskins, B. J., I. Draghici and H. C. Davies. 1978. A new look at the ω-equation. Quart. J. Roy. Meteor. Soc., *104,* 31–38.

Hua, B. L. 1994. Skewness of the generalized centrifugal force divergence for a joint normal distribution of strain and vorticity components. Phys. Fluids, *A6,* 3200-3202.

Hua, B. L. and D. Haidvogel. 1986. Numerical simulations of the vertical structure of quasi-geostrophic turbulence. J. Atmos. Sci., *43,* 2923–2936.

Hua, B. L. and P. Klein. 1998. An exact criterion for the stirring properties of nearly two-dimensional turbulence. *Physica D, 113,* 98-110.

Hua, B. L., J. McWilliams and P. Klein. 1998. Lagrangian accelerations in geostrophic turbulence. J. Fluid Mech., (in press).

MacVean, M. K. and J. D. Woods. 1980. Redistribution of scalars during upper frontogenesis: A numerical model. Quart. J. Roy. Meteor. Soc., *106,* 293–311.

Okubo, A. 1970. Horizontal dispersion of floatable particles in the vicinity of velocity singularities such as convergence. Deep-Sea Res., *17,* 445–454.

Park, Y. H. and L. Gamberoni. 1997. Cross-frontal exchange of Antarctic Intermediate Water and Antarctic Bottom Water in the Crozet Basin. Deep-Sea Res., *44,* 963–986.

Rhines, P. B. 1983. Lectures in geophysical fluid dynamics, *in* Lectures in Applied Mathematics, *20,* 3–58.

Roden, G. I. 1977. Oceanic subarctic fronts of the central Pacific: Structure of and response to atmospheric forcing. J. Phys. Oceanogr., *7,* 761–778.

Weiss, J. 1991. The dynamics of enstrophy transfer in two-dimensional hydrodynamics. Physica D, *48,* 273–294; [see also Weiss, J. 1981. Report LJI-TN-81-121, La Jolla Inst., San Diego, CA].

Yuan, X. and L. D. Talley. 1992. Shallow salinity minimum in the North Pacific. J. Phys. Oceanogr., *22,* 1302–1316.